

Joint Channel Measurement and Simulation Analysis in an L-shaped Indoor Hallway in the Terahertz Band

Yiqin Wang, Yuanbo Li, Chong Han, *Member, IEEE*, Yi Chen, and Ziming Yu

Abstract

The Terahertz (THz) band (0.1-10 THz), which supports Terabit-per-second (Tbps) data rates, has been envisioned as one of the promising spectrum bands for sixth-generation (6G) and beyond communications. In this paper, an angular-resolvable wideband channel measurement campaign in an indoor L-shaped hallway at 306-321 GHz is presented, by using a frequency-domain vector network analyzer (VNA)-based channel sounder. Four line-of-sight (LoS), six quasi-line-of-sight (QLoS) and eight non-line-of-sight (NLoS) receiver points are measured. However, measured data spreads due to the rich scattering environment and the antenna pattern, which puzzles traditional clustering algorithms. To solve this problem, a simulation-assisted Density-Based Spatial Clustering of Applications with Noise (DBSCAN) clustering algorithm is proposed, where the deterministic simulation result is extracted to adapt the conventional DBSCAN algorithm. The proposed algorithm outperforms conventional clustering algorithms like DBSCAN, K-means, and K-power-means in terms of Silhouette, Calinski-Harabasz and Davies-Bouldin indices. Furthermore, the THz multi-path propagation in the L-shaped hallway is elaborated, and channel characteristics of multipath and clusters are analyzed in depth.

Index Terms

Terahertz communications, 6G and beyond, Channel measurement, Clustering.

I. INTRODUCTION

Rapid growth of the wireless data traffic in the past decades has stimulated the demand for 100 Gigabit-per-second and even Terabit-per-second (Tbps) communications in future wireless appli-

This paper was presented in part at the IEEE ICC, 2022 [1].

Yiqin Wang, Yuanbo Li, and Chong Han are with the Terahertz Wireless Communications (TWC) Laboratory, Shanghai Jiao Tong University, Shanghai, China (e-mail: {wangyiqin, yuanbo.li, chong.han}@sjtu.edu.cn).

Yi Chen, and Ziming Yu are with Huawei Technologies Co., Ltd, China (e-mail: {chenyi171, yuziming}@huawei.com).

cations. Compared with the millimeter-wave (mmWave) band (30-300 GHz) that has bandwidth of several gigahertz (GHz), the Terahertz (THz) band (0.1-10 THz), which can support Tbps data rates owing to multi-tens-of-GHz bandwidth, has been envisioned as one of the promising spectrum bands for sixth-generation (6G) and beyond communications [2], [3]. When moving up to new spectrum, the foundation of wireless system design is the full knowledge of wireless channels, including understanding of radio propagation, channel characteristics analysis, and channel model development.

On one hand, physical channel measurement supported by a wideband channel sounder is one of the major approaches to investigate THz wireless channels [4]. Due to the high path loss and frequency-dependent molecular absorption above 300 GHz, to-date THz channel measurement campaigns, typically, either focused on the “sub-THz” band (100-300 GHz) [5]–[10], or line-of-sight (LoS) [11]–[13] and short-range (desktop, motherboard, data center) [14], [15] scenarios above 300 GHz. Though, there are THz channel measurements at and above 300 GHz in a larger-scale environment implemented in a small (about 10 m²) indoor office room [16], an urban microcell scenario [17], railway or vehicular communication scenarios [18], [19], and indoor hallway scenarios [1], [20].

On the other hand, channel simulation is another way to study THz wireless channels, which is typically implemented for channel characteristic analysis in the environment where measurement is unavailable [21], or for channel data reproduction [4]. To-date channel simulators rely on deterministic channel modeling methods, like CloudRT [22], [23], EDX Advanced Propagation [24], and Wireless InSite [25], or stochastic, like QuaDriGa [26] and NYUSIM [27], [28]. Among them, deterministic simulators can provide the same channel parameters as the measurement based on geometric theories, and can further provide information on the trajectory of wave propagation. Though simulation is more efficient than physical channel measurement, its accuracy is vulnerable to the discrepancy between the simulation model and the real environment, including the detailed geometry, exact material properties, and antenna array patterns.

In light of the fact that channel measurement and simulation are two approaches to study the channel, joint analysis of measurement and simulation in the same environment is worth of exploration. For instance, measurement data is used to validate simulation results and extract material properties [29], [30]. Furthermore, in channel modeling, the deterministic part in a hybrid channel model can be generated by ray-tracing (RT) simulators, while the statistical part is extracted from measurement data [5]. However, in these studies, the analysis of the

measurement data is independent of the simulation result.

In this paper, we conduct joint channel measurement and simulation analysis, where the deterministic simulation result is utilized to guide the clustering of measurement data. Since measured data spreads due to rich scattering and the antenna pattern, and thus puzzles traditional clustering algorithms, we bring in deterministic simulation results to find reference cluster centers and help match and locate clusters in the measurement dataset. The key idea is, by invoking the explicit physical meaning of the deterministic simulation results into the measurement data clustering, the conventional clustering algorithm is adapted for channel measurement peculiarities, and thus, both the performance and the credibility of the clustering result are improved. In particular, we first present an angular-resolvable wideband channel measurement campaign conducted in a typical indoor L-shaped hallway at 306-321 GHz with a frequency-domain vector network analyzer (VNA)-based channel sounder. Four points in the LoS case, six points in the quasi-line-of-sight (QLoS) case and eight points in the non-line-of-sight (NLoS) case are measured.

Then, we implement the simulation in Wireless InSite and propose a simulation-assisted clustering algorithm, which is adapted from the Density-Based Spatial Clustering of Applications with Noise (DBSCAN) algorithm. The performance of the proposed algorithm outperforms conventional clustering algorithms like DBSCAN, K-means, and K-power-means (KPM), in terms of validation metrics, i.e., Silhouette index, Calinski-Harabasz index and Davies-Bouldin index. In light of power delay angular profiles (PDAPs) of the measurement and results of the proposed algorithm, the multi-path propagation in the THz band in the L-shaped hallway scenario is traced and analyzed meticulously. Finally, we analyze the indoor THz channel characteristics including path loss, delay spread and angular spreads, and intra-cluster spreads in depth. Compared to our preliminary and shorter version [1], this work includes the development and validation of a simulation-assisted DBSCAN algorithm, and the analysis of multi-path propagation and clustering effects for the wireless THz channel in the L-shaped hallway indoor scenario. The distinctive contributions of this work are summarized as follows.

- An angular-resolvable wideband channel measurement campaign is conducted with a frequency-domain VNA-based channel sounder and an RT-based simulation is implemented through Wireless InSite in the same indoor L-shaped hallway at 306-321 GHz. Eighteen receiver (Rx) positions are investigated, including LoS, QLoS and NLoS cases.
- The significance of the joint channel measurement and simulation analysis is elaborated, by using the same output parameters of the simulation and the measurement. Remarkably,

the deterministic simulation provides information on wave propagation trajectories, and provides explicit physical meaning into the statistical process of the measurement data, which improves both the performance and the credibility of the data post-processing result.

- A simulation-assisted, DBSCAN-based clustering algorithm is proposed to cluster multi-path components (MPCs) extracted from the measurement. The proposed algorithm is designed for channel measurement peculiarities, and outperforms conventional DBSCAN, K-means and KPM algorithm in terms of three validation metrics, namely, Silhouette, Calinski-Harabasz and Davies-Bouldin indices.
- A comprehensive analysis of indoor channel characteristics is provided. In particular, the large-scale fading, delay spread, angular spreads, cluster number, and intra-cluster characteristics are analyzed. THz channel characteristics in the indoor L-shaped hallway scenarios are compared in depth between LoS, QLoS, and NLoS cases.

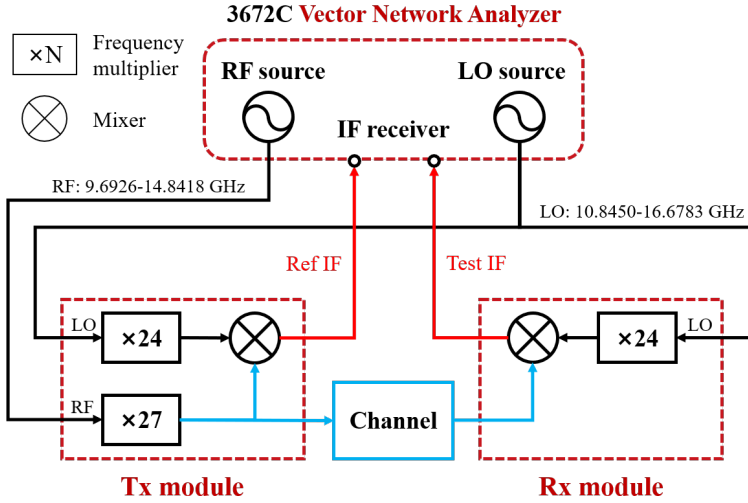
The remainder of this paper is organized as follows. In Sec. II, the channel measurement campaign and the MPC extraction procedure are introduced. In Sec. III, we carry out simulation of the same environment in Wireless InSite, and propose a simulation-assisted DBSCAN-based clustering algorithm. In Sec. IV, we elaborate the multi-path propagation in the L-shaped hallway. Furthermore, indoor channel characteristics, including the large-scale fading, delay spread, angular spreads, and cluster-related characteristics are also analyzed in depth. Finally, the paper is concluded in Sec. V.

II. CHANNEL MEASUREMENT CAMPAIGN

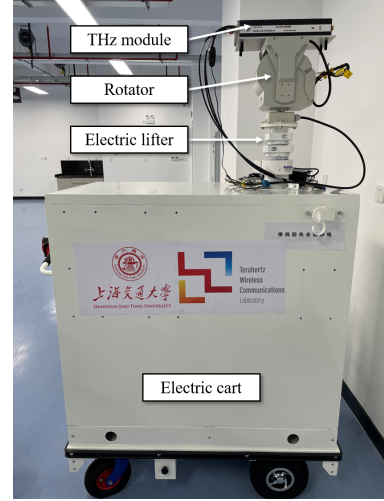
In this section, we describe the 306-321 GHz measurement campaign as well as the data post-processing procedures in the L-shaped hallway. The measurement is carried out on the second floor of the Longbin building, at the University of Michigan-Shanghai Jiao Tong University Joint Institute (UM-SJTU JI), Shanghai Jiao Tong University (SJTU).

A. Channel Measurement System

We adopt a 260-400 GHz channel measurement platform that consists of radio frequency (RF) fronts supported by a Ceyear 3672C VNA, as illustrated in Fig. 1(a). The VNA supports the frequency range from 10 MHz to 43.5 GHz. Standard waveguides WR2.8 are integrated with both Tx and Rx modules, while a horn antenna is installed at the Rx side. The Tx waveguide has a gain of around 7 dBi, while the Rx antenna has a half-power beamwidth (HPBW) of 8° .



(a) The RF front of the channel measurement system.



(b) The photo of the channel measurement system.

Fig. 1: Channel measurement system.

and an antenna gain around 25-27 dBi at 260-400 GHz. In this measurement campaign, the frequency band of 306-321 GHz is investigated. The measured bandwidth is 15 GHz, which denotes that the time and space resolutions are 66.7 ps and 2 cm, respectively. The frequency sweeping interval is 2.5 MHz, resulting in 6001 sweeping points and a maximum excess delay of 400 ns, which is equivalent to a maximum detectable path length of 120 m. The noise floor of the THz measurement platform is -180 dBm, and the dynamic range is 119 dB.

As shown in Fig. 1(b), the transceiver module is mounted on a rotator. The Tx is placed on an electric lifter, which is integrated with the electric cart, to reach the height of 2 m above the ground. By contrast, the Rx is put on the top of the cart without a lifter, which results in the height of 1.75 m above the ground. The Tx is static at zero azimuth and elevation angles. Motored by the rotator, the Rx scans from 0° to 360° in the azimuth domain and from -20° to 20° in the elevation domain to receive multi-path propagation, with the angle step of 10° . Key parameters of the measurement system are summarized in Table I.

B. Measurement Deployment

The measurement campaign is conducted in the L-shaped hallway on the second floor of the building of UM-SJTU JI. As shown in Fig. 2(a), the campaign mainly consists of two perpendicular corridors, connected by a corner. The long corridor is 2.97 m wide and 32.53 m

TABLE I: Parameters of the measurement system.

Parameter	Value
Frequency band	306-321 GHz
Bandwidth	15 GHz
Sweeping interval	2.5 MHz
Sweeping points	6001
Tx antenna gain	7 dBi
Rx antenna gain	25-27 dBi
HPBW of Rx antenna	8°
Time resolution	66.7 ps
Space resolution	2 cm
Maximum excess delay	400 ns
Maximum path length	120 m
Rx azimuth rotation range	[0° : 10° : 360°]
Rx elevation rotation range	[-20° : 10° : 20°]
Average noise floor	-180 dBm
Dynamic range	119 dB

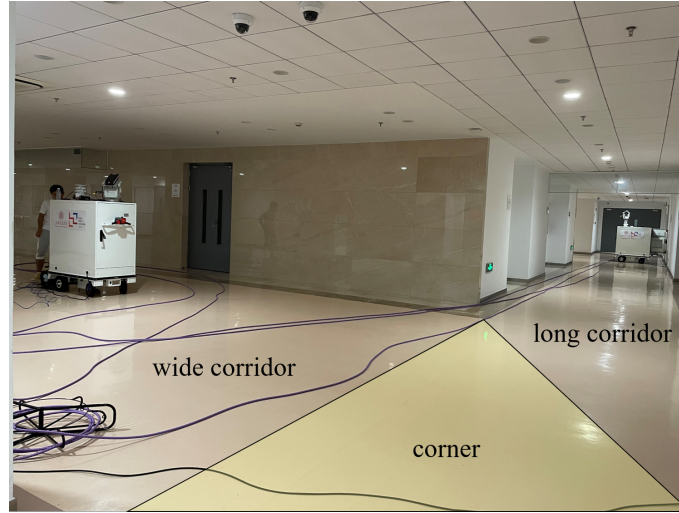
long (between Wall A and Wall B), including two 3 m long extensions at both ends. Indented offices are distributed along the corridor, whose depth is about 0.6 m with doors closed. The other corridor is 7 m wide (between Wall C and Wall D) which extends all the way to the left end. The measurement deployment is illustrated in Fig. 2(b). Tx is placed in the long corridor, together with four LoS Rx positions, while six QLoS and eight NLoS Rx positions are located in the wide corridor. Since signals are too weak to be detected in the wide corridor far from the corner, the rest of the wide corridor to the left end is omitted in Fig. 2(b).

C. MPC Extraction

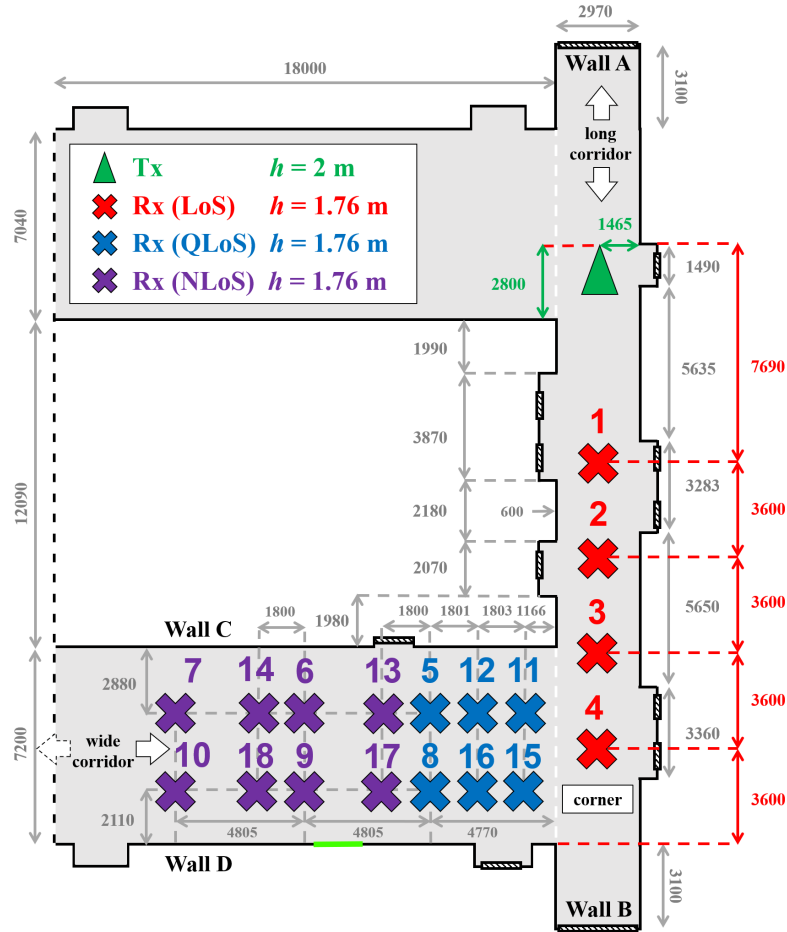
Before data processing, system calibration is carried out to eliminate the effect of the measurement system [6]. For each Tx-Rx direction pair, we obtain 6001 samples of channel impulse response (CIR) h_{channel} from the inverse discrete Fourier transform (IDFT) of the channel transfer function (CTF) H_{channel} . We regard each sample as one possible MPC in the temporal domain and eliminate noise samples whose power are lower than the threshold, given by

$$P_{\text{TH}} [\text{dB}] = \max\{P_{\text{m}} - 40, \text{NF} + 10\}, \quad (1)$$

where P_{m} denotes the maximum power among measured samples, and NF is the average noise floor. After noise elimination, the azimuth and elevation angles of the Rx are considered as the



(a) The photo of the measurement campaign.



(b) Measurement deployment (unit: mm).

Fig. 2: Measurement campaign and deployment in an L-shaped hallway, 2nd floor of UM-SJTU JI building, SJTU.

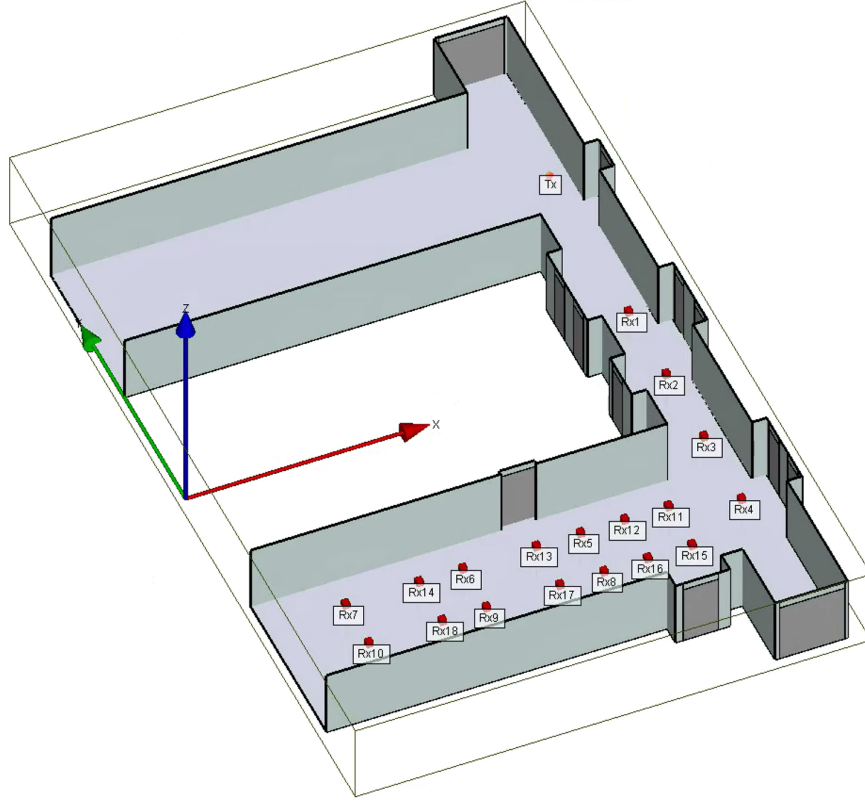


Fig. 3: Simulation deployment.

azimuth and elevation angles-of-arrival (AoA, EoA) of each MPC, respectively. The delay of receiving the sample is equal to the time-of-arrival (ToA) of the corresponding MPC.

III. SIMULATION-ASSISTED DBSCAN CLUSTERING ALGORITHM

In this section, we introduce and verify the proposed simulation-assisted DBSCAN clustering algorithm. First, in Sec. III-A, we carry out the simulation. The significance and the drawback of simulation are also discussed. On account of the comparison between measurement and simulation, we extract the delay and angular information from both datasets and propose the simulation-assisted DBSCAN clustering algorithm, which is introduced in Sec. III-B. At last, in Sec. III-C, we verify the clustering result by comparing its performance with the counterparts of conventional clustering algorithms like DBSCAN, K-means, and KPM.

A. Simulation

The simulation is implemented in Wireless InSite, with the deployment depicted in Fig. 3. The simulation results are used to assist the clustering of the measurement data for the following

reasons.

First, the RF propagation software can simulate EM propagation and provides channel characteristics in indoor environments. The output includes the direction of departure, the direction of arrival, the time of arrival, and the received power, which accord with those derived from the measurement data. Therefore, it enables parallel or combined analysis of results from the measurement and the simulation. Moreover, the RT simulator provides the traveling path of each ray, including the number and positions of interactions, which has explicit physical meaning. This advantage over the measurement provides additional information in helping identify scatterers in the environment.

Nevertheless, the power values given by the simulation result is not credible due to the following facts: (a) The floor plan is simplified; (b) the accurate antenna pattern is unavailable; (c) the scattering effect is inaccurate owing to the uncertainty of precise models for every kind of materials at the target frequency band [23].

Therefore, we omit the power of each ray given by the simulation, and instead, use the delay and angular information to assist the clustering of the measurement data. We adopt the Lambertian diffuse scattering model, in which the incident field scatters evenly in directions around the normal direction of the surface. We then extract two thousand rays for each Tx-Rx pair in the simulation, which are adequate to cover major multi-path components. Besides, the traveling paths traced in the simulation are used to analyze the multi-path propagation in the environment.

B. Simulation-assisted DBSCAN Algorithm

As illustrated in Fig. 4, we first process raw data from the measurement. After this step, the main part of the proposed clustering algorithm is divided into three parts, namely, interference elimination, combined clustering, and simulation-assisted clustering.

Before the implementation of the algorithm, since the measurement data is affected by the receiver antenna pattern, we compress the measurement data to reserve major MPCs in the spatial domain. As a result, components that result from the sidelobes due to the antenna pattern are removed. To be specific, at each time point, n measured power data are represented in $\mathbb{D} = [d_1, d_2, \dots, d_n]^T$. The antenna pattern is denoted by $\mathbf{c} = [c_1, c_2, \dots, c_{2p+1}]^T$ ($2p + 1 \leq n$), where c_{p+1} is relative antenna gain at zero boresight angle, i.e., the ratio of the antenna gain at zero boresight angle to the reference Rx antenna gain in Table I. c_1 to c_p denote relative antenna

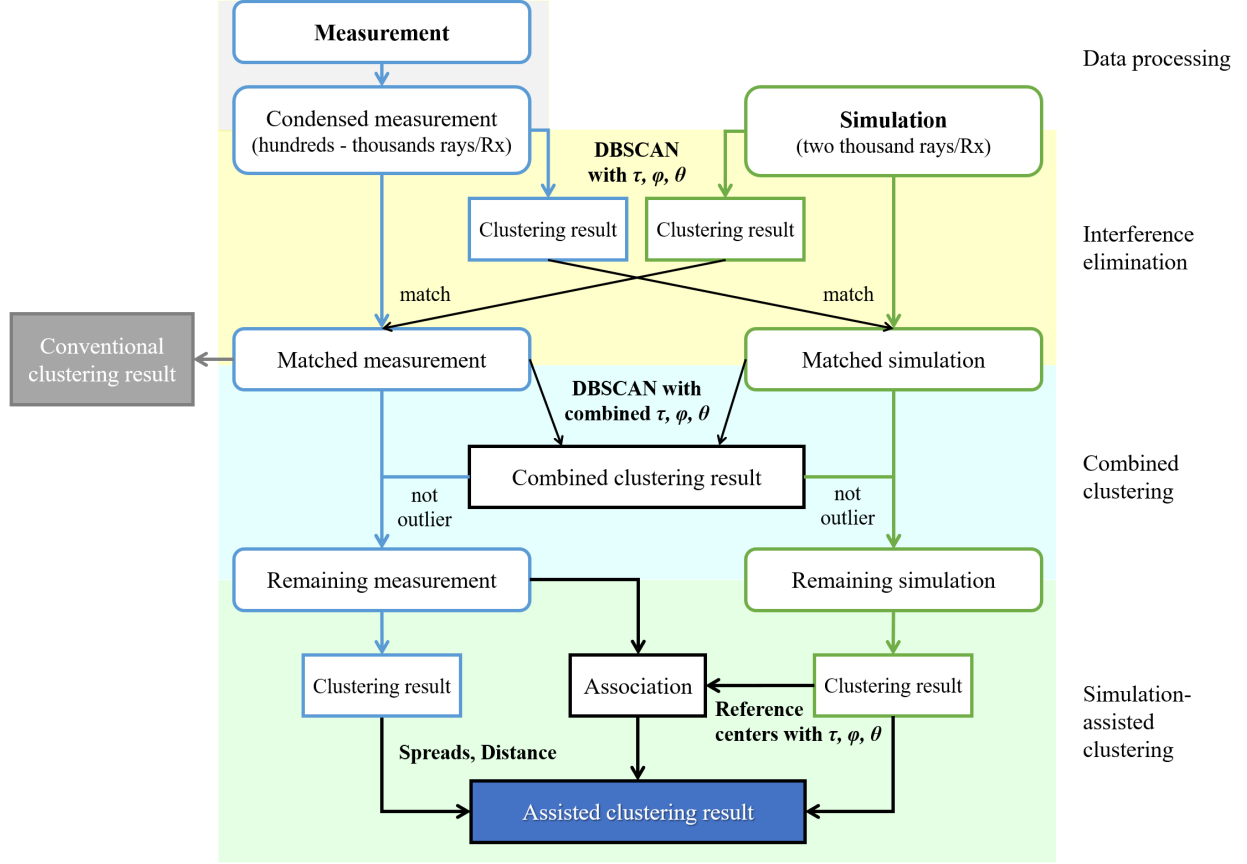


Fig. 4: Flow chart of the simulation-assisted DBSCAN clustering algorithm.

gains from the negative cutoff angle to the smallest negative resolvable angle. c_{p+2} to c_{2p} denote relative antenna gains from the smallest positive resolvable angle to the positive cutoff angle. We estimate the condensed power data $\mathbb{X} = [x_1, x_2, \dots, x_n]^T$, which simulates the MPC power distribution without the influence of the antenna pattern, by invoking the n -by- n convolution matrix $\mathbb{C} = [\mathbf{c}_1, \dots, \mathbf{c}_n]$. The column \mathbf{c}_{p+1} is the zero-pad version of \mathbf{c} , and \mathbf{c}_{i+1}^T is the right cyclic shift of \mathbf{c}_i^T . The condensed power data is estimated by

$$\mathbb{X} = \operatorname{argmin} \|\mathbb{C}\mathbb{X} - \mathbb{D}\|_2^2. \quad (2)$$

Then, the following algorithm is based on the multi-path component distance (MCD)-based DBSCAN clustering algorithm [5], with extra assistance of the simulation dataset. In particular, MCD is defined as

$$MCD = \sqrt{d^2 + \xi d_\tau^2}, \quad (3)$$

where ξ indicates the weight of temporal difference. d and d_τ represent the distances between two MPCs in the spatial and temporal domains, respectively, described as

$$d = \left\| \begin{pmatrix} \cos(\theta_i) \cdot \cos(\varphi_i) - \cos(\theta_j) \cdot \cos(\varphi_j) \\ \cos(\theta_i) \cdot \sin(\varphi_i) - \cos(\theta_j) \cdot \sin(\varphi_j) \\ \sin(\theta_i) - \sin(\theta_j) \end{pmatrix} \right\|_2, \quad (4a)$$

$$d_\tau = |\tau_i - \tau_j| / \tau_m, \quad (4b)$$

where $\theta_{i/j}$ and $\varphi_{i/j}$ represent the elevation and azimuth AoA the i/j -th MPC, $\tau_{i/j}$ is the ToA of the i/j -th MPC, and τ_m denotes the maximum ToA among all MPCs. Therefore, MPCs with similar ToA, AoA, and EoA are grouped into clusters based on the DBSCAN algorithm.

After data processing, redundant MPCs in two datasets are first filtered out through *interference elimination* and *combined clustering*. Then, the adapted clustering algorithm is implemented in *simulation-assisted clustering*, which finds reference cluster centers from simulation results and then help locate clusters in the measurement dataset.

1) *Interference elimination*: Both simulation and condensed measurement data are filtered with respect to the other dataset, respectively, in order to eliminate interference. In the measurement, the interference comes from objects that are unrelated with the scenario, for instance, electric carts of the measurement platform. In the simulation, clusters of simulated MPCs that are not detected by measurement are also eliminated, for instance, clusters of MPCs from the left end of the wide corridor. In view of possible mismatches between the simulation and the measurement, we only abandon clusters in which none of MPCs is close to any MPC in the other dataset. Therefore, the rough filtering can reserve true MPCs in the environment as much as possible, which still tolerates a small amount of interfering clusters.

2) *Combined clustering*: After interference elimination, two matched datasets are combined into one large dataset and clustered by DBSCAN. Compared with respective clustering in the last step, in combined clustering, the range of the cluster (determined by parameter ϵ) is reduced. As a result, a small number (determined by parameter *MinPts*) of MPCs at the edge of clusters which cannot form a cluster are identified as outliers and thus filtered out by combined clustering.

3) *Simulation-assisted clustering*: After combined clustering, the remaining MPCs in simulation are divided into clusters, whose centers are extracted as a hint about major MPCs in measurement. The adapted DBSCAN algorithm first set these reference centers as the core point

of each cluster, and visit the data points in the ϵ -neighborhood of core points, respectively. When a neighbor is visited, it is recursively set as the core point if it has at least a minimum number ($MinPts$) of neighbors. At this step, visited measurement data are not directly assigned to these clusters. Instead, this step obtains how each measurement data point is associated with clusters that are initialized by the centers. Since the original DBSCAN algorithm recursively expands clusters based on their neighbors, each data point can be reached by, or associated with (a) no cluster, (b) one cluster, or (c) more than one clusters. If a data point is associated with only one cluster, the cluster number is assigned. Otherwise, both the data and the center are labelled as unassigned and passed to the next step. A measurement data point can be associated with more than one clusters in one of the following situations. First, measured data is spread and can be reached by ϵ -neighborhood of multiple centers. Second, measured data is additionally reached by unassociated centers whose positions are imprecise due to the mismatch between the measurement and the simulation. Besides, the mismatch can also give rise to unassigned measurement data which are not associated with any of the clusters. Therefore, at the next step, unassigned data are first by themselves clustered with traditional DBSCAN. Then, for each cluster of unassigned data, by thresholding two factors, i.e., temporal and spatial spreads and distances from unassigned centers, the algorithm makes distinction between the aforementioned situations.

C. Verification

To evaluate the quality of the clustering result, two kinds of validation metrics are normally used, i.e., external indices and internal indices. An external index measures the agreement between the result given by the clustering algorithm and the prior-known clustering structure (or the true label). By contrast, an internal index measures the goodness of a clustering result purely based on inherent features of the data set, without having access to any external information.

In the scope of channel measurement, the “true label” of MPC clusters is hardly accessible for the following reasons. First of all, the concept of cluster evolves from the observation of MPCs which arrive in the form of clusters at the receiver side [31]. Though the concept of cluster is well accepted and applied in statistical channel modeling, the essence of channel responses is still embedded in MPCs rather than clusters. In this sense, theoretically, the “true label” of the cluster structure is not applicable. On the other hand, the “true label” (or reference) of the cluster structure can be generated by existing channel models (or simulators) [32]. However, the

credibility of the reference is highly dependent on the agreement between the actual measuring environment and the model. As existing models are generalized to be applied to a certain type of scenarios, specific characteristics of the actual environment are typically weakened or omitted. Therefore, the use of existing general models as the reference is not fair. Furthermore, the measuring data is susceptible to the measurement resolution, the antenna pattern, and the calibration process [33].

Therefore, in this case, it is more suitable to evaluate the clustering result of the proposed algorithm with internal indices, and compare them with the counterparts of conventional clustering algorithms like DBSCAN, K-means, and KPM. The clustering performance of four clustering algorithms on measured MPCs are evaluated by the following three common internal indices.

1) The *Silhouette Index (SI)* for each sample is defined as

$$S_i = \frac{b_i - a_i}{\max(a_i, b_i)}, \quad (5)$$

where a_i denotes the mean distance between the i -th sample and all other samples in the same cluster, and b_i is the mean distance between the i -th sample and all other samples in the next nearest cluster. The SI for a set of samples is given as the mean of SI values for each sample, as

$$SI = \frac{1}{n} \sum_{i=1}^n S_i, \quad (6)$$

where n is the number of MPCs. The score is bounded between -1 and +1. A high SI score indicates that clusters are dense and well separated.

2) The *Calinski-Harabasz (CH)* index, also known as the variance ratio criterion, is defined as

$$CH = \frac{\text{tr}(B_k)}{\text{tr}(W_k)} \times \frac{n - k}{k - 1}, \quad (7)$$

where the data set of size n is clustered into k clusters. B_k is the between-cluster dispersion matrix, and W_k is the within-cluster dispersion matrix. Dispersion is defined as the sum of squared distances. The two dispersion matrices are defined as

$$B_k = \sum_{q=1}^k n_q (c_q - c)(c_q - c)^T, \quad (8a)$$

$$W_k = \sum_{q=1}^k \sum_{x \in C_q} (x - c_q)(x - c_q)^T, \quad (8b)$$

where c is the center of all data samples, and C_q denotes the set of samples in the q -th cluster, with size n_q and center c_q . A high CH score indicates that clusters are dense and well separated.

3) The *Davies-Bouldin (DB)* index, in the contrary, measures the average “similarity” between clusters, where the similarity is defined as

$$R_{ij} = \frac{s_i + s_j}{d_{ij}}, \quad (9)$$

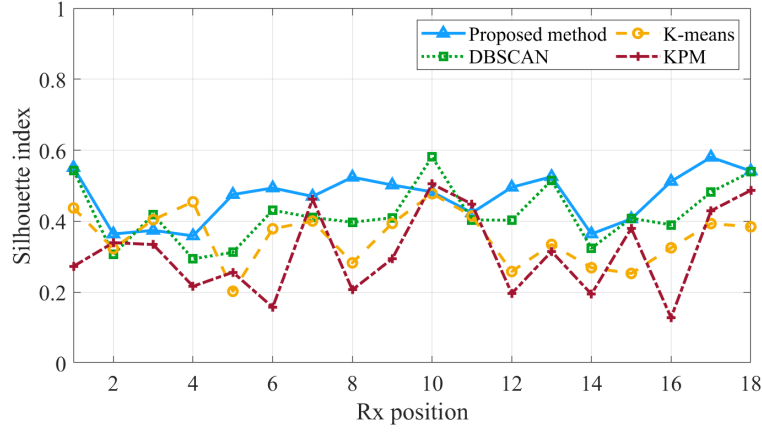
where s_i indicates the average distance between each sample in the i -th cluster and the center of this cluster, and d_{ij} is the distance between the centers of the i -th and the j -th clusters. The DB index is then derived as the average “similarity” between each cluster C_i and its most similar cluster C_j , as

$$DB = \frac{1}{k} \sum_{i=1}^k \max_{j \neq i} R_{ij}. \quad (10)$$

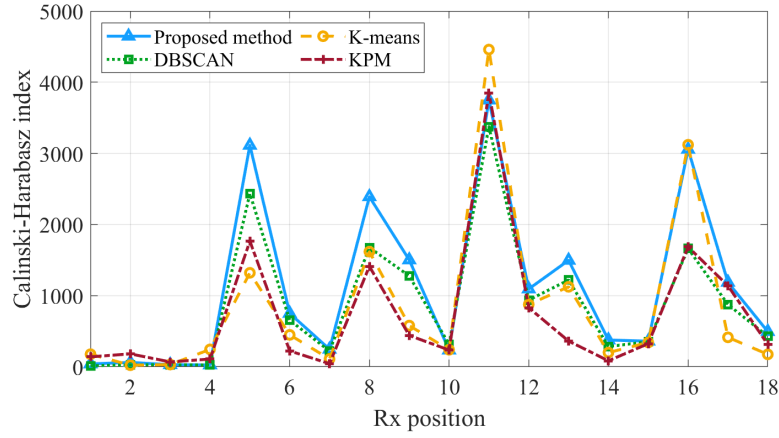
The DB index is lower bounded by zero, and a low DB score indicates a good clustering result.

Fig. 5 shows the performance of the proposed simulation-assisted clustering algorithm and conventional clustering algorithms like DBSCAN, K-means, and KPM. In terms of three internal indices, in general, the proposed method performs the best among four clustering algorithms. First, though the MPC distribution over time and spatial domains varies with Rx positions, especially between LoS and NLoS conditions, the proposed method manages to retain stable with high SI, high CH and low DB scores. Second, the proposed method performs particularly well at Rx5, Rx8, Rx12, and Rx16, where the clustering complexity is high on account of the huge amount of non-noise MPCs, i.e., thousands of MPCs at these Rx positions compared with hundreds of MPCs at others. As the the number of MPCs increases, especially in the QLoS case, MPCs are crowded together and are more likely to be mixed by conventional clustering algorithms. By contrast, the proposed clustering algorithm invokes the physical meaning given by the deterministic simulation result, and therefore, guarantees good clustering performance.

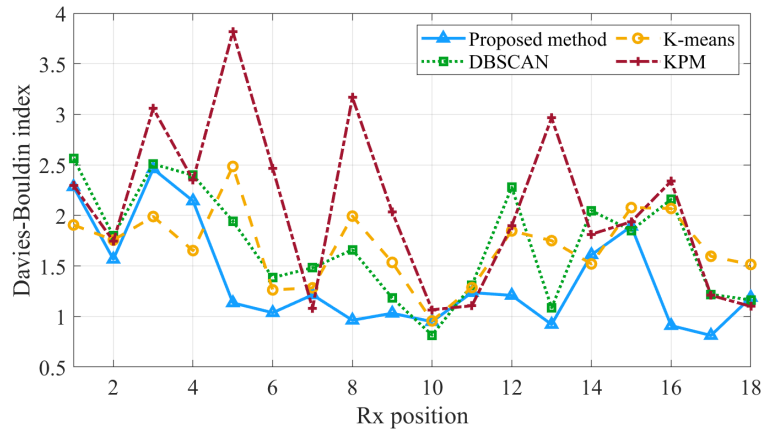
Conventional clustering algorithms have disadvantages in clustering of the channel measurement dataset. First, K-means and KPM (a) require the preset of the number of clusters, k , (b) are sensitive to initial cluster centers and optimized according to internal indices, (c) cannot distinguish outliers, and (d) are more suitable for convex datasets. In the proposed algorithm, we



(a) Clustering performance in terms of SI.



(b) Clustering performance in terms of CH.



(c) Clustering performance in terms of DB.

Fig. 5: Clustering performance of the proposed algorithm, DBSACN, K-means, and KPM, evaluated by (a) SI, (b) CH, and (c) DB.

obtain the number of clusters in a deterministic way, and set this number as k in K-means and KPM. To be fair, we statistically initialize initial cluster centers according to the distributions of MPCs in both temporal and spatial domains, and choose the best result among ten trials in terms of internal indices. By contrast, DBSCAN (a) does not need the pre-knowledge of k , (b) is independent of initial cluster centers, (c) can distinguish outliers, and (d) supports arbitrary cluster shapes. However, the peculiarity of THz channel measurement datasets, where measured data spread and mix up due to rich scattering and the antenna pattern, puzzles the clustering algorithm. Specifically, the number of clusters is confused, and cluster characteristics as well. Therefore, we adapt the algorithm for THz channel measurement data clustering by invoking deterministic simulation results as the guidance for locating clusters. Furthermore, though the self-adapting algorithm is not optimized in terms of internal indices as K-means and KPM, the result still verifies its performance.

IV. CHANNEL ANALYSIS AND CHARACTERIZATION

In this section, the multi-path propagation in two corridors of the L-shaped hallway is traced and analyzed meticulously. Furthermore, channel characteristics are analyzed in depth, including path loss (PL), delay spread (DS) and azimuth spread of angle (ASA), and elevation spread of angle (ESA). Besides, channel characteristics associated with the clustering result, i.e., cluster number, intra-cluster delay spread and angular spreads, are compared between the original DBSCAN algorithm and the proposed simulation-assisted DBSCAN algorithm in Sec. III-B.

A. Multi-path Propagation Analysis

In this part, we analyze the multi-path propagation in two corridors of the L-shaped hallway based on PDAPs and clustering results.

1) *LoS case*: We first take Rx1 in the LoS case as an example, and analyze the spatial and temporal distributions of MPCs in the LoS indoor hallway scenario. As shown in Fig. 6, cluster 1 denotes the cluster consisting of the LoS ray and some scattering paths, with the largest cluster power and the ToA of 26 ns, i.e., the travelling distance of 7.8 m. Cluster 2, which travels 8.4 m, are reflected from the wall. Cluster 3, 4, 5, and 6 are reflected from the indented offices distributed along the corridor. As shown in Fig. 6(a) and (b), the values of the azimuth AoA and the ToA are in well accordance with the office locations in the campaign. Besides, cluster 7 results from the reflections between the two electric carts of Tx and Rx. This is verified by the

value of ToA 77 ns, which is about three times the ToA of the LoS cluster, i.e., the MPCs are reflected by the carts twice and travel three times the distance between the Tx and the Rx, as shown in Fig. 6(b). Cluster 8 represents the first-order reflection by one end of the long corridor, for which the ToA of 143 ns indicates the traveling distance of 43 m. By contrast, Cluster 9, which immediately follows Cluster 8, travels 48 m, and possibly refers to the reflected rays from the floor and the ceiling. Furthermore, Cluster 10 is the second-order reflection by two ends of the long corridor. The ToA of 246 ns indicates the traveling distance of 73.8 m, which is larger than that of the LoS cluster by 56 m, about twice the length of the long corridor.

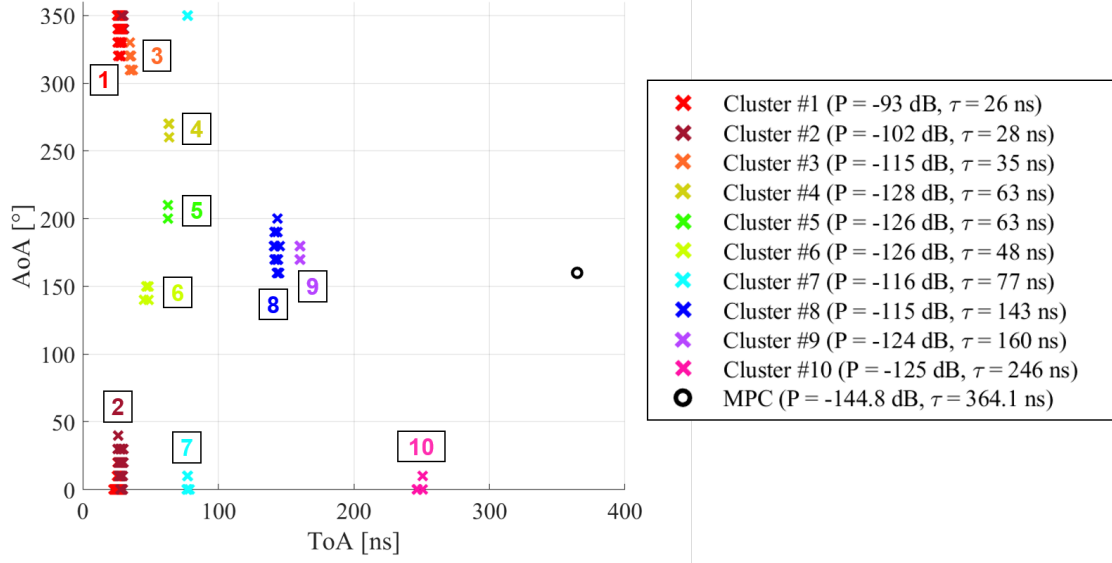
Note that there exists an MPC arriving from Wall B at 364 ns, which travels about 109 m. The MPC, which does not form a cluster, though, is reflected three times between Wall A and Wall B. The power of the MPC is -144.8 dB, on account of the strong reflection by Wall A and Wall B, which are actually metal doors.

2) *QLoS and NLoS cases*: First, in QLoS and NLoS cases where the LoS ray is absent, MPCs mainly come from the corner of two corridors and travel at least 17 m to reach the QLoS points near the corner. The strong MPC received at QLoS Rx has the path loss smaller than 125 dB, while the value is typically larger than 130 dB at NLoS Rx. Besides, far NLoS MPCs traveling a long distance (more than 60 m in our case) are too weak to be detected.

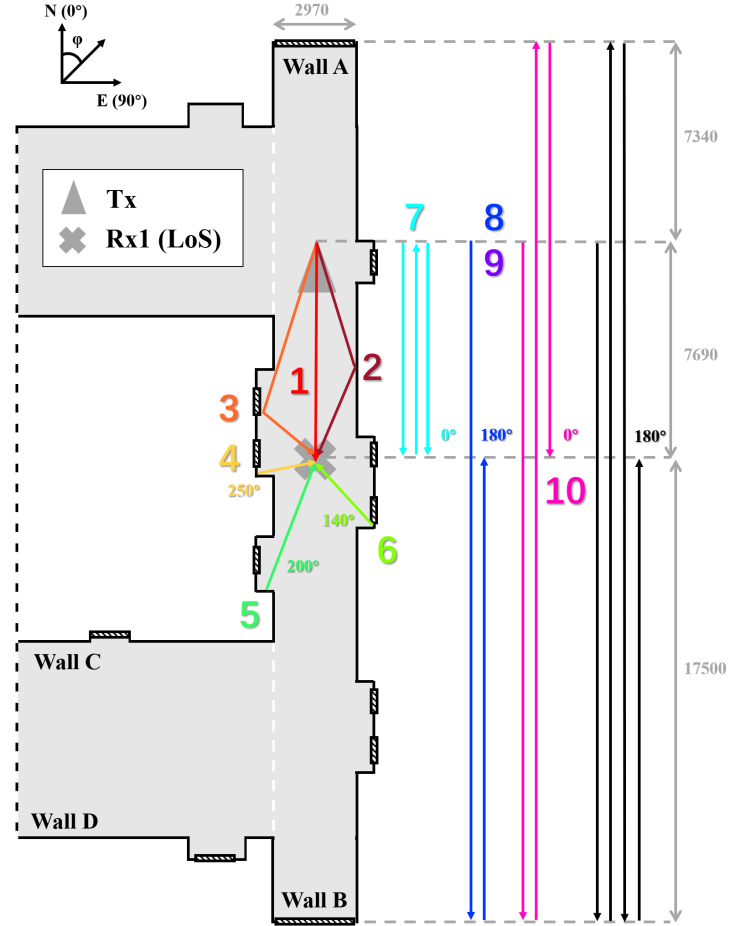
Then, we take Rx5 to Rx7 as examples and analyze the spatial and temporal distributions of MPCs in the wide corridor. The PDAP results are shown in Fig. 7. The majority of MPCs are concentrated in the azimuth AoA ranging from 0 to 180° and the ToA ranging from 75 to 200 ns. We mainly explore the trend of MPCs. In specific, as the Rx position farther away from the corner (i.e., from Rx5 to Rx7), intuitively, MPCs travel a longer distance and thus have larger ToAs. At the same time, azimuth AoAs tend to converge towards $\varphi = 90^\circ$ (the white dotted lines in Fig. 7), which is the direction pointing perpendicular to the long corridor. The observation gives a clue for the existence of fixed scattering points on Wall C and Wall D adjacent to the corner, for instance, the two indented metal doors.

B. Characteristic Analysis

1) *Path loss*: The path loss is divided into best direction path loss and omni-directional path losses. For each pair of Tx and Rx positions, the best direction path loss is defined as the loss of the MPC from the best direction which has the strongest received power. By contrast, the



(a) Clustering result at Rx1.



(b) Multi-path analysis at Rx1 (unit: mm).

Fig. 6: Clustering result and multi-path analysis at Rx1.

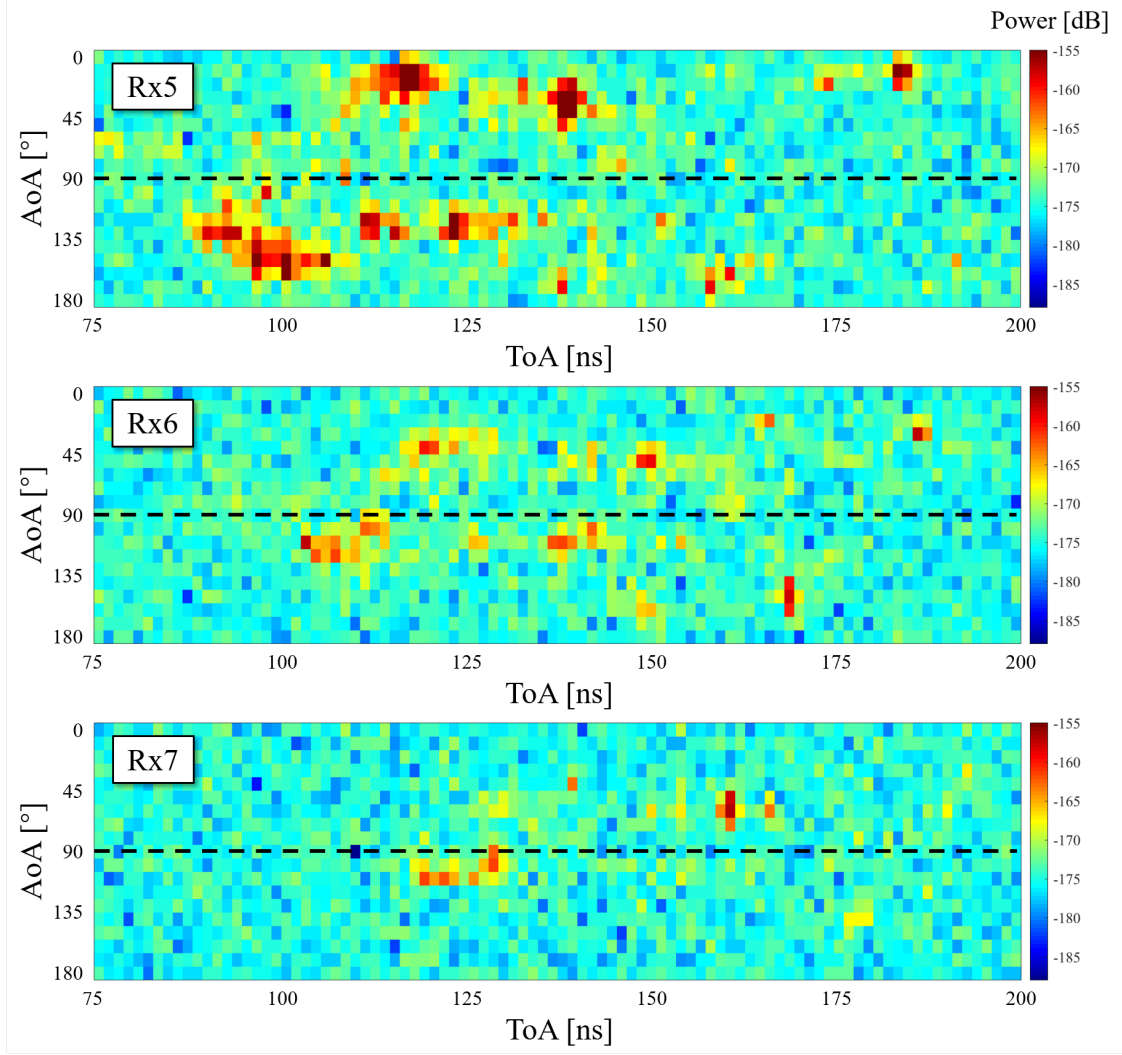


Fig. 7: Measured PDAP at Rx5, Rx6, and Rx7.

omni-directional path loss sums the received power from all directions. The two path losses are respectively given by

$$PL_{\text{best}} [\text{dB}] = -10 \cdot \log_{10} \left(\max_{i,j} \{P_{i,j}\} \right), \quad (11a)$$

$$PL_{\text{omni}} [\text{dB}] = -10 \cdot \log_{10} \left(\sum_{i,j} P_{i,j} \right), \quad (11b)$$

where $P_{i,j}$ denotes the received power from the i^{th} azimuth angle and the j^{th} elevation angle, as

$$P_{i,j} = \sum_t |h_{i,j,t}|^2, \quad (12)$$

TABLE II: Summary of channel characteristics.

Characteristics		LoS				QLoS						NLoS							
		Rx1	Rx2	Rx3	Rx4	Rx5	Rx8	Rx11	Rx12	Rx15	Rx16	Rx6	Rx7	Rx9	Rx10	Rx13	Rx14	Rx17	Rx18
Distance [m]		7.69	11.29	14.89	18.49	18.84	20.95	17.96	18.32	20.17	20.49	20.93	23.83	22.86	25.53	19.51	21.94	21.56	23.78
Angular spreads [°]	ASA	19.96	29.04	31.52	52.11	42.50	52.72	38.83	51.72	20.27	68.08	66.99	44.36	62.81	29.55	60.26	79.34	62.48	40.24
	lg ASA	1.30	1.46	1.50	1.72	1.63	1.72	1.59	1.71	1.31	1.83	1.83	1.65	1.80	1.47	1.78	1.90	1.80	1.60
	μ lgASA	1.49				1.63						1.73							
	σ lgASA	0.15				0.16						0.13							
	ESA	6.78	6.29	6.09	6.46	6.14	7.71	4.89	7.64	6.11	7.53	6.23	5.01	5.38	4.69	8.09	4.27	7.17	5.71
	lg ESA	0.83	0.80	0.78	0.81	0.79	0.89	0.69	0.88	0.79	0.88	0.79	0.70	0.73	0.67	0.91	0.63	0.86	0.76
	μ lgESA	0.81				0.82						0.76							
	σ lgESA	0.02				0.07						0.09							
Delay spread [ns]	DS	10.86	22.41	21.10	21.90	21.87	40.00	20.11	28.88	7.12	29.09	58.22	36.45	29.96	29.56	22.35	63.30	23.49	33.28
	lgDS	-7.96	-7.65	-7.68	-7.66	-7.66	-7.40	-7.70	-7.54	-8.15	-7.54	-7.23	-7.44	-7.52	-7.53	-7.65	-7.20	-7.63	-7.48
	μ lgDS	-7.74				-7.66						-7.46							
	σ lgDS	0.13				0.24						0.16							
K-factor	K	18.09	13.18	13.74	8.95	NaN						NaN							
	μ K	13.49																	
	σ K	3.24																	
Path loss & shadow fading [dB]	PL _{best}	95.65	99.12	101.37	105.43	123.25	114.63	111.76	120.59	108.50	119.35	141.23	147.13	121.42	144.41	134.33	143.49	130.26	145.31
	μ PL _{best}	100.39				116.35						138.45							
	PLE _{best}	1.66				2.64						4.16							
	σ SF _{best}	3.55				5.17						8.40							
	PL _{omni}	91.63	95.62	98.99	101.02	118.64	108.99	110.10	115.30	105.82	114.32	133.67	140.16	117.58	139.26	127.63	135.55	125.03	139.29
	μ PL _{omni}	96.82				112.20						132.27							
	PLE _{omni}	1.34				2.31						3.70							
	σ SF _{omni}	3.56				4.30						7.61							

where $h_{i,j,t}$ represents the CIR at the t^{th} sample time point from, the i^{th} azimuth and the j^{th} elevation angles.

The close-in free space reference distance (CI) model is invoked based on the results of best direction and omni-directional path losses, respectively. The CI path loss model is expressed as

$$\text{PL}^{\text{CI}} = 10 \times \text{PLE} \times \log_{10} \frac{d}{d_0} + \text{FSPL}(d_0) + X_{\sigma_{\text{SF}}}, \quad (13)$$

where PLE is the path loss exponent, d denotes the distance between Tx and Rx, and d_0 , which is 1 m in this work, represents the reference distance. $X_{\sigma_{\text{SF}}}$ is a zero-mean Gaussian random variable with standard deviation σ_{SF} in dB, indicating the fluctuation caused by shadow fading. Furthermore, the free-space path loss (FSPL) is given by the Friis' law, as

$$\text{FSPL}(d, f) = -20 \times \log_{10} \frac{c}{4\pi f d}, \quad (14)$$

where f denotes the frequency, and c is the speed of light. We determine the values of PLE in

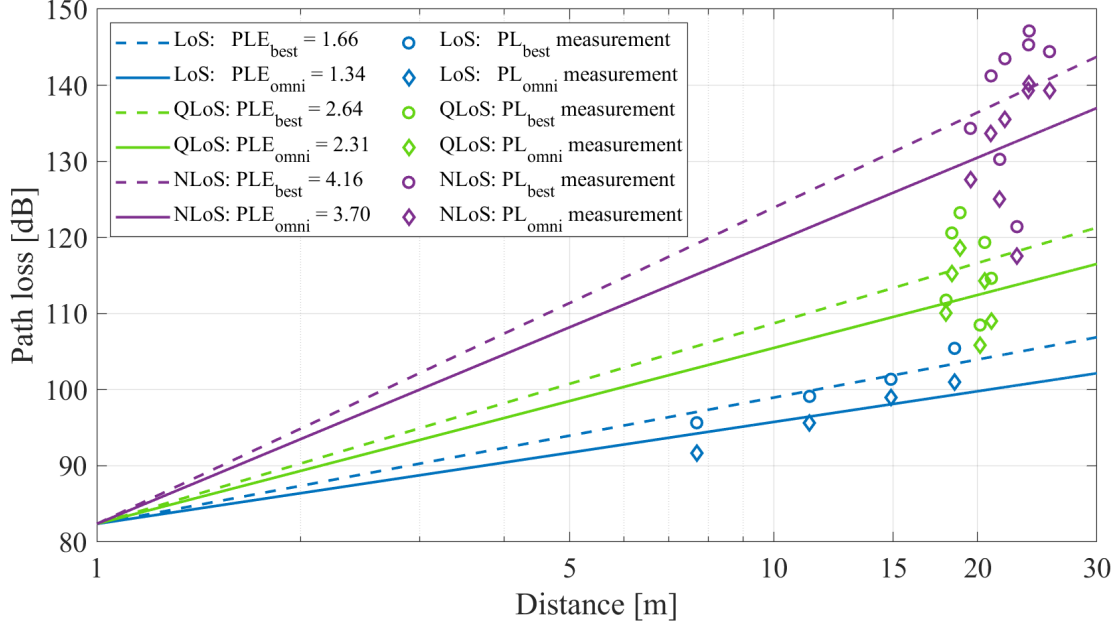


Fig. 8: Path loss measurement and fitted CI models.

the CI model by minimizing σ_{SF} .

The fitting results are shown in Fig. 8 and summarized in Table II. The measurement results yield that the PLE value is 1.66 for the best direction path loss and 1.34 for the omni-direction path loss, respectively, in the LoS case. Justifications are elaborated as follows. First, due to the waveguide effect, besides the LoS ray, strong reflected paths with different ToAs can also be detected from the best direction. Thus, the received power is increased by the summation of received power in the *time* domain, as expressed in (12). As a result, the best direction path loss is reduced, and the PLE value is smaller than 2, which is the PLE for ideal free-space path loss. Second, the omni-directional received power sums the received power in both *time* and *angular* domains. To be specific, besides paths from the best direction, reflected paths from the south, and scattered paths from all other directions are included in the summation of (12), resulting in a smaller PLE for the omni-directional path loss. In QLoS and NLoS cases, the values of Tx-Rx distances are relatively concentrated. We obtain higher path losses at Rx positions in QLoS and NLoS cases and thus higher PLEs for both kinds of path losses.

2) *Delay and angular spreads*: We use the root-mean-square (RMS) delay spread and angular spreads to measure the power dispersion of MPCs in temporal and spatial domains, respectively. The results are summarized in Table II. In the LoS case, the values of DS are around 20 ns,

except for Rx1 due to the reflection from offices, as illustrated in Fig. 6. The value of ASA increases as the position of Rx moves closer to the corner, which is caused by MPCs which are reflected and scattered between the corner and the cart. These MPCs arrive at the Rx with the azimuth AoA around 180° . As a result, the increase of received power from the south (with φ near 180°) counterweights the power of MPCs from the north (with φ near 0° or 360°), and results in a larger ASA. The average DS and ASA are 19.07 ns and 33.16° in the LoS case.

In QLoS and NLoS cases, since most MPCs have power comparable to the noise floor, values of DS and ASA are highly dependent on the dominated MPCs. At the QLoS Rx positions, the low values at the best direction path loss indicate the existence of high-power reflected MPCs, which are dominant in QLoS case. When Rx moves farther away into NLoS positions, these MPCs become weaker and are overwhelmed by scattering MPCs between Wall C and Wall D. Furthermore, some MPCs are buried in the noise, which renders inconclusive changes of DS and ASA. Though, in the general sense, the average DS and ASA are 24.51 ns and 45.69° in the QLoS case, and 37.08 ns and 55.75° in the NLoS case, which are larger than the counterparts in the LoS case.

C. Cluster-related Characteristics

The number of clusters, intra-cluster delay spread (CDS), intra-cluster azimuth spread of angle (CASA) and intra-cluster elevation spread of angle (CESA) are summarized in Table III. The results of the classical DBSCAN algorithm and the proposed simulation-assisted DBSCAN algorithm are enumerated respectively.

1) *Number of clusters*: For both algorithms, the number of cluster does not vary drastically in the LoS case. Besides, in the QLoS case which is near the corner, due to the abundant reflecting and scattering, the cluster number is larger than that in the LoS case, despite the lack of the LoS ray. By contrast, when the Rx position moves farther into the NLoS case, the cluster number decreases due to the larger path loss. In general, clusters are most abundant in the QLoS case, followed by the NLoS case and then the LoS case. The average number of cluster is 9 and 10.27 given by the classical DBSCAN and the proposed algorithm, respectively. The reason is elaborated as follows. In the measurement, MPCs are spread in the angular domain due to the scattering and the antenna pattern. Therefore, the classical DBSCAN tends to mix up several separate clusters into one large cluster. By contrast, the proposed algorithm utilizes the information given by the simulation to distinguish these clusters apart. At the same time,

TABLE III: Summary of cluster-related channel characteristics.

Characteristics		LoS				QLoS						NLoS							
		Rx1	Rx2	Rx3	Rx4	Rx5	Rx8	Rx11	Rx12	Rx15	Rx16	Rx6	Rx7	Rx9	Rx10	Rx13	Rx14	Rx17	Rx18
Cluster-related characteristics with the original DBSCAN algorithm																			
Cluster number	N	9	6	8	6	11	18	9	18	6	16	10	4	7	7	8	9	11	6
	μ_N	7.25				13.00						7.75							
	σ_N	1.30				4.62						2.11							
Intra-cluster ASA [°]	μ_{CASA}	5.25				4.73						4.87							
	σ_{CASA}	4.05				3.67						3.04							
Intra-cluster ESA [°]	μ_{CESA}	4.32				4.26						4.34							
	σ_{CESA}	1.93				2.44						2.17							
Intra-cluster DS [ns]	μ_{CDS}	0.80				2.38						2.33							
	σ_{CDS}	0.58				2.57						2.16							
Cluster-related characteristics with the proposed simulation-assisted DBSCAN algorithm																			
Cluster number	N	9	6	8	9	13	16	9	19	8	14	12	7	9	8	14	9	8	7
	μ_N	8.00				13.17						9.25							
	σ_N	1.22				3.80						2.33							
Intra-cluster ASA [°]	μ_{CASA}	5.07				3.90						4.11							
	σ_{CASA}	3.47				3.03						2.98							
Intra-cluster ESA [°]	μ_{CESA}	4.67				4.97						3.66							
	σ_{CESA}	1.88				2.46						2.45							
Intra-cluster DS [ns]	μ_{CDS}	0.55				0.87						0.70							
	σ_{CDS}	0.47				0.72						0.59							

the guidance of the simulation prevents the proposed algorithm from cheating by excessively dividing the measurement results into many small clusters.

2) *Intra-cluster delay spread and angular spreads*: The quality of the clustering result of the proposed algorithm can also be verified by intra-cluster characteristics. As illustrated in Table III and Fig. 9(a), in average, the proposed algorithm results in smaller delay spreads and azimuth angular spreads inside each cluster in LoS, QLoS and NLoS cases, which means MPCs in each cluster are more concentrated. Moreover, as illustrated in Table III and Fig. 9(b), the deviations of CDS and CASA also become smaller in all three cases, which indicate that the clustering performance of the proposed algorithm is more stable in every case, compared with the classical DBSCAN algorithm. Besides, since we do not scan the whole elevation space in this campaign, the results of CESA are not conclusive.

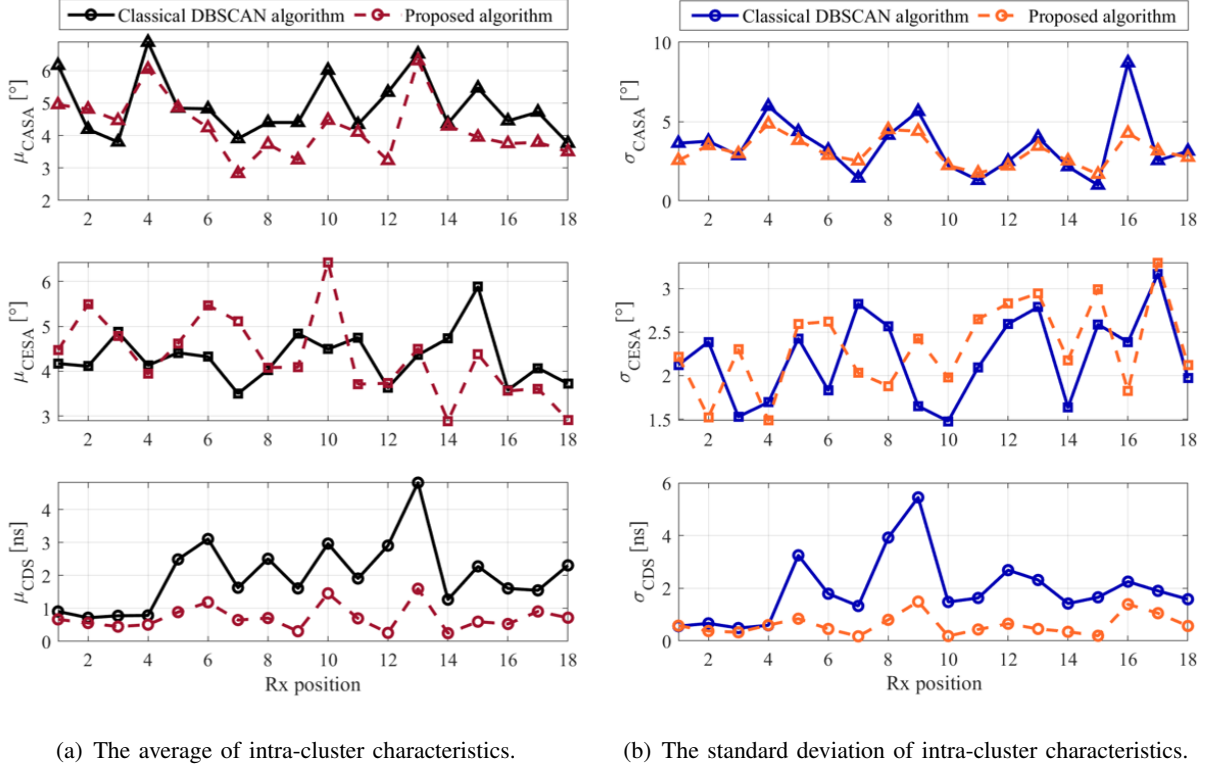


Fig. 9: Comparison of the average and the standard deviation of intra-cluster characteristics (CASA: intra-cluster azimuth spread of angle, CESA: intra-cluster elevation spread of angle, CDS: intra-cluster delay spread).

V. CONCLUSION

In this paper, we have conducted joint channel measurement and simulation analysis, where the deterministic simulation result is utilized to guide the clustering of measurement data. First, we completed an angular-resolvable wideband channel measurement and simulation in an indoor L-shaped hallway at 306-321 GHz. The measurement is carried out by using a frequency-domain VNA-based channel sounder, while the simulation is implemented in Wireless InSite. Then, we proposed an adapted DBSCAN algorithm, which is assisted by the hint of delay and angular distributions of MPCs given by the simulation result. The proposed algorithm outperforms conventional clustering algorithms like DBSCAN, K-means, and KPM in terms of three validation metrics, and reduces the deviation of spreads inside clusters.

The multi-path propagation in the hallway is traced and analyzed in terms of PDAPs and clustering results. Indoor THz channel characteristics including path loss, delay spread and angular spreads are analyzed as summarized in Table II and III. Specifically, the PLEs are

1.66 for the best direction path loss and 1.34 for the omni-directional path loss in the LoS case. The power dispersion of MPCs in both temporal and azimuth angular domains is the smallest, 19.07 ns and 33.16° , in the LoS case, followed by 24.51 ns and 45.69° in the QLoS case, and 37.08 ns and 55.75° in the NLoS case. The average cluster numbers are 8, 13, and 9 in LoS, QLoS, and NLoS cases, respectively.

Compared with the indoor office scenario in the mmWave and lower frequency bands [34], the indoor L-shaped hallway scenario at 306-321 GHz has smaller path loss and delay spread in the LoS case and large ones in the NLoS case. By contrast, the azimuth angular spread is increased in every case. Besides, the cluster numbers are greatly decreased in overall cases.

REFERENCES

- [1] Y. Wang, Y. Li, Y. Chen, Z. Yu, and C. Han, "0.3 THz Channel Measurement and Analysis in an L-shaped Indoor Hallway," in *Proc. of IEEE International Conference on Communications (ICC)*, pp. 1–6, Jun. 2022.
- [2] I. F. Akyildiz, C. Han, Z. Hu, S. Nie, and J. M. Jornet, "Terahertz band communication: An old problem revisited and research directions for the next decade," *IEEE Transactions on Communications*, vol. 70, no. 6, pp. 4250–4285, 2022.
- [3] T. S. Rappaport, Y. Xing, O. Kanhere, S. Ju, A. Madanayake, S. Mandal, A. Alkhateeb, and G. C. Trichopoulos, "Wireless Communications and Applications Above 100 GHz: Opportunities and Challenges for 6G and Beyond," *IEEE Access*, vol. 7, pp. 78 729–78 757, Jun. 2019.
- [4] C. Han, Y. Wang, Y. Li, Y. Chen, N. A. Abbasi, T. Kürner, and A. F. Molisch, "Terahertz wireless channels: A holistic survey on measurement, modeling, and analysis," *IEEE Communications Surveys & Tutorials*, to appear, 2022.
- [5] Y. Chen, Y. Li, C. Han, Z. Yu, and G. Wang, "Channel Measurement and Ray-Tracing-Statistical Hybrid Modeling for Low-Terahertz Indoor Communications," *IEEE Transactions on Wireless Communications*, vol. 20, no. 12, pp. 8163–8176, 2021.
- [6] J. He, Y. Chen, Y. Wang, Z. Yu, and C. Han, "Channel Measurement and Path-Loss Characterization for Low-Terahertz Indoor Scenarios," in *Proc. of IEEE ICC Workshops*, pp. 1–6, Jun. 2021.
- [7] S. L. H. Nguyen, K. Haneda, J. Järveläinen, A. Karttunen, and J. Putkonen, "Large-Scale Parameters of Spatio-Temporal Short-Range Indoor Backhaul Channels at 140 GHz," in *Proc. of IEEE VTC*, pp. 1–6, Apr. 2021.
- [8] N. A. Abbasi, J. Gomez-Ponce, R. Kondaveti, A. Kumar, E. Bhagat, R. N. S. Rao, S. Abu-Surra, G. Xu, C. Zhang, and A. F. Molisch, "Double-Directional Channel Measurements for Urban THz Microcellular Communications in a Street Canyon," in *Proc. of IEEE International Conference on Communications (ICC)*, pp. 1–6, May 2022.
- [9] S. Ju, Y. Xing, O. Kanhere, and T. S. Rappaport, "Sub-Terahertz Channel Measurements and Characterization in a Factory Building," in *Proc. of IEEE International Conference on Communications (ICC)*, pp. 1–6, May 2022.
- [10] D. Dupleich, R. Müller, S. Skoblikov, M. Landmann, G. Del Galdo, and R. Thomä, "Characterization of the Propagation Channel in Conference Room Scenario at 190 GHz," in *Proc. of EuCAP*, pp. 1–5, Jul. 2020.
- [11] Y. Zantah, F. Sheikh, A. A. Abbas, M. Alissa, and T. Kaiser, "Channel measurements in lecture room environment at 300 GHz," in *Proc. of IWMTS*, pp. 1–5, Jul. 2019.
- [12] N. Khalid, N. A. Abbasi, and O. B. Akan, "Statistical characterization and analysis of low-THz communication channel for 5G Internet of Things," *Nano Communication Networks*, vol. 22, p. 100258, Dec. 2019.

- [13] D. Serghiou, M. Khalily, S. Johny, M. Stanley, I. Fatadin, T. Brown, N. Ridler, and R. Tafazolli, "Ultra-Wideband Terahertz Channel Propagation Measurements from 500 to 750 GHz," in *Proc. of International Conference on UCET*, pp. 1–4, Aug. 2020.
- [14] S. Kim and A. Zajić, "Characterization of 300-GHz Wireless Channel on a Computer Motherboard," *IEEE Transactions on Antennas and Propagation*, vol. 64, no. 12, pp. 5411–5423, Oct. 2016.
- [15] J. M. Eckhardt, T. Doeker, S. Rey, and T. Kürner, "Measurements in a real data centre at 300 GHz and recent results," in *Proc. of EuCAP*, pp. 1–5, Apr. 2019.
- [16] S. Priebe, C. Jastrow, M. Jacob, T. Kleine-Ostmann, T. Schrader, and T. Kürner, "Channel and propagation measurements at 300 GHz," *IEEE Transactions on Antennas and Propagation*, vol. 59, no. 5, pp. 1688–1698, Mar. 2011.
- [17] F. Undi, A. Schultze, W. Keusgen, M. Peter, and T. Eichler, "Angle-Resolved THz Channel Measurements at 300 GHz in an Outdoor Environment," in *Proc. of IEEE ICC Workshops*, pp. 1–7, Jun. 2021.
- [18] K. Guan, D. He, B. Ai, Y. Chen, C. Han, B. Peng, Z. Zhong, and T. Kürner, "Channel Characterization and Capacity Analysis for THz Communication Enabled Smart Rail Mobility," *IEEE Transactions on Vehicular Technology*, vol. 70, no. 5, pp. 4065–4080, Apr. 2021.
- [19] J. M. Eckhardt, V. Petrov, D. Moltchanov, Y. Koucheryavy, and T. Kürner, "Channel Measurements and Modeling for Low Terahertz Band Vehicular Communications," *IEEE Journal on Selected Areas in Communications*, vol. 39, no. 6, pp. 1590–1603, Apr. 2021.
- [20] Y. Li, Y. Wang, Y. Chen, Z. Yu, and C. Han, "Channel Measurement and Analysis in an Indoor Corridor Scenario at 300 GHz," in *Proc. of IEEE International Conference on Communications (ICC)*, pp. 1–6, Jun. 2022.
- [21] J. Yang, H. Li, and Z. Xu, "Analysis of channel characteristics between satellite and space station in terahertz band based on ray tracing," *Radio Science*, vol. 56, no. 9, pp. 1–16, 2021.
- [22] L. Wang, K. Guan, B. Ai, G. Li, D. He, R. He, L. Tian, J. Dou, and Z. Zhong, "An accelerated algorithm for ray tracing simulation based on high-performance computation," in *Proc. of International Symposium on Antennas, Propagation and EM Theory (ISAPE)*, pp. 512–515, Oct. 2016.
- [23] D. He, B. Ai, K. Guan, L. Wang, Z. Zhong, and T. Kürner, "The Design and Applications of High-Performance Ray-Tracing Simulation Platform for 5G and Beyond Wireless Communications: A Tutorial," *IEEE Communications Surveys & Tutorials*, vol. 21, no. 1, pp. 10–27, Aug. 2019.
- [24] "EDX Advanced Propagation," <http://edx.com/products/advanced-propagation-module/>.
- [25] "RECOM Wireless InSite," <https://www.remcom.com/wireless-insite-em-propagation-software/>.
- [26] S. Jaeckel, L. Raschkowski, K. Börner, L. Thiele, F. Burkhardt, and E. Eberlein, "QuaDriGa - Quasi Deterministic Raio Channel Generator, User Manual and Documentation," Fraunhofer Heinrich Hertz Institute, Technical Report (TR), Oct. 2020, version 2.4.0.
- [27] S. Sun, G. R. MacCartney, and T. S. Rappaport, "A novel millimeter-wave channel simulator and applications for 5G wireless communications," in *Proc. of IEEE International Conference on Communications (ICC)*, pp. 1–7, May 2017.
- [28] "NYUSIM 3.0, Indoor channel simulator up to 150 GHz," <https://wireless.engineering.nyu.edu/nyusim/>.
- [29] H. Yi, K. Guan, D. He, B. Ai, J. Dou, Z. Lai, and Z. Zhong, "Terahertz channel measurement and characterization on a desktop from 75 to 400 GHz," in *Proc. of IEEE International Conference on Electronic Information and Communication Technology (ICEICT)*, pp. 756–761, 2021.
- [30] K. Guan, B. Peng, D. He, J. M. Eckhardt, S. Rey, B. Ai, Z. Zhong, and T. Kürner, "Measurement, simulation, and characterization of train-to-infrastructure inside-station channel at the terahertz band," *IEEE Transactions on Terahertz Science and Technology*, vol. 9, no. 3, pp. 291–306, 2019.

- [31] Saleh, A. M. A., Valenzuela, and R., "A Statistical Model for Indoor Multipath Propagation," *IEEE Journal on Selected Areas in Communications*, Feb. 1987.
- [32] Y. Chen, C. Han, J. He, and G. Wang, "A Framework of Mahalanobis-Distance Metric with Supervised Learning for Clustering Multipath Components in MIMO Channel Analysis," *IEEE Transactions on Antennas and Propagation*, vol. 70, no. 6, pp. 4069–4081, Jun. 2022.
- [33] X. Yin, L. Ouyang, and H. Wang, "Performance Comparison of SAGE and MUSIC for Channel Estimation in Direction-Scan Measurements," *IEEE Access*, vol. 4, pp. 1163–1174, Mar. 2016.
- [34] 3GPP, "Study on channel model for frequencies from 0.5 to 100 GHz," 3rd Generation Partnership Project (3GPP), Technical Report (TR) 38.901, Dec. 2019, version 16.1.0.